Permeability anisotropy systematically deflects fluid flow in volcanic media

Jamie I. Farquharson[1*]

[1]Institute for Research Administration, Niigata University, Ikarashi 2-8050, Nishi-Ku, Niigata, 950-2181, Japan

Corresponding author: Jamie I. Farquharson (jfarquharson@gs.niigata-u.ac.jp)
Orcid: 0000-0003-4933-2607

This is a non-peer reviewed preprint submitted to EarthArXiv. This preprint has also been submitted to a journal for peer review.

EarthArXiv preprint

Permeability anisotropy systematically deflects fluid flow in volcanic media

Jamie I. Farquharson[1*]

[1]Institute for Research Administration, Niigata University, Ikarashi 2-8050, Nishi-Ku, Niigata, 950-2181, Japan

Corresponding author: Jamie I. Farquharson (jfarquharson@gs.niigata-u.ac.jp)
Orcid: 0000-0003-4933-2607

Key Points:

- Volcanic permeability is directionally dependent.
- Anisotropy can deflect fluid flow away from the pressure gradient, except when flow is parallel or perpendicular to structural fabric.
- Fluid deflection can evolve with deformation, and can control the pathways for volcanic fluid flow and location of surface gas discharge.

EarthArXiv preprint

Abstract

Permeability is fundamental in volcanic systems, governing heat and mass transfer across spatial scales and controlling pressurisation of the edifice and conduit. In nature, permeability is rarely isotropic and should be treated as a second-order tensor rather than a scalar. This contribution experimentally demonstrates directional dependence of permeability in transversely isotropic volcanic tuff, highlighting a critical phenomenon: other than when measurements are made parallel or perpendicular to fabric (the structural axis **n**), flow is deflected away from the driving hydraulic gradient. A closed-form analytical expression is derived for the critical gradient angle β^*, which describes the hydraulic gradient orientation relative to **n** at which flow deflection reaches its maximum value δ^*. The angle β^* depends only on the permeability anisotropy ratio. This effect has consequences for the interpretation of volcanic fluid pathways: anisotropy can decouple surface fluid discharge from the direction of the driving pressure gradient, produce lateral offsets between subsurface sources and surface expressions, and allow permeability anisotropy to be inferred from flow trajectories. Changes in anisotropy during deformation or compaction can further significantly redirect preferential flow pathways through time.

Plain Language Summary

The capacity for fluid to move through rocks inside a volcano controls how the volcano builds pressure and how heat and mass are transferred through the system, and the parameter that describes this is *permeability*. Although often permeability is considered to be the same in all directions, in reality there are many active processes inside a volcano which cause permeability to be higher in one direction than another by creating a direction-dependent structure or fabric. Using a volcanic rock which demonstrates this phenomenon, measurements of permeability are made at multiple different angles. The results are used to highlight some key insights, notably that the direction that fluid actually flows can differ from the direction of the pressure pushing the fluid. The amount of this deflection depends on the rock's permeability in different directions. Equations shown here allow the identification of the pressure direction that produces the biggest deflection. This has important implications for understanding volcanic fluid movement. Fluids released at the surface, for example through steaming fumaroles, may not come from directly from the point beneath them where the pressure is generated. Instead, differences in the rock's permeability can make fluids move sideways as well as upwards, creating an offset between sources and surface emissions. Finally, because deformation can change the rock's permeability, the pathway that fluids prefer to travel along can also change substantially over time.

EarthArXiv preprint

1 Introduction

Permeability—the capacity for fluid flow through a porous or granular medium—is a fundamental process-limiting crustal property [1,2]. It governs heat and mass transfer in the crust [3], and controls the generation of supra-hydrostatic pressures in volcanoes [4,5], in turn modulating explosive hazards [6–8]. Permeable architecture can be structured at different scales, from the pore network [9,10] to regional-scale fault

systems [11,12]; its orientation and anisotropy ultimately determines the fate of fluids. Permeability anisotropy in volcanic rocks may reach several orders of magnitude [13–16], demonstrating a first-order effect of orientation-dependence.

Permeability is often treated as an isotropic scalar property, implicitly requiring the pore network to be statistically equivalent in all directions. More generally, it is a symmetric positive-definite second-order tensor K_{ij} (equivalently, $\mathbf{K}$) that relates the pressure gradient $\partial p/\,\partial x_j$ of a fluid with viscosity μ to the Darcy flux q_i through the relation $q_i = -\mu^{-1} K_{ij}\,\partial p/\,\partial x_j$ [17,18]. Isotropy requires that $\mathbf{K}$ remains unchanged irrespective of reorientation of the medium which forces $\mathbf{K} = k\mathbf{I}$ ($k > 0$ is the scalar permeability, $\boldsymbol{I}$ the identity tensor). $\mathbf{K}$ has six independent components; the isotropic form fixes all six via a single parameter making isotropy a special measure-zero subset of the constitutive space. An intermediate case (characterised by four components) is transverse isotropy, in which a dominant structural axis $\mathbf{n}$ exists in the pore network. $\mathbf{K}$ inherits the symmetry of the pore network [18,19], so any deviatoric deformation that modifies pore geometry perturbs $\mathbf{K}$ away from isotropy. Magma shear [20–23], vesicle elongation [24], crystal fabric development [25], fracturing [26,27], bubble interaction [28], or compaction [14] can all systematically reduce pore-space symmetry in volcanic systems, suggesting that permeability anisotropy—commonly of axisymmetric, transversely isotropic form—is the expected consequence of deformation.

The transverse isotropic case is described by $\mathbf{K} = k_\perp(\boldsymbol{I} - \mathbf{n} \otimes \mathbf{n}) + k_\parallel \mathbf{n} \otimes \mathbf{n}$, with two independent permeability values perpendicular ($k_\perp$) and parallel ($k_\parallel$) to fabric. This is consistent with mutually orthogonal permeability measurements in volcanic rocks and magmas with structural fabrics [9,13,14,29–32]. However, measurements are not always made parallel or perpendicular to fabric, so the tensor may be sampled at arbitrary orientations. Permeability can be recovered by rotation of the principal tensor through the angle subtended between $\mathbf{n}$ and the measurement direction.

In a coördinate system xyz, the value of a tensor property at angle θ from the principal axes can be found by rotating the coördinate frame by θ, giving a new system $\bar{x}\bar{y}\bar{z}$. For a transversely isotropic medium, $x = y \neq z$ with k_x and k_z corresponding to $k_\perp$ and $k_\parallel$. The rotation is:

$$\begin{bmatrix} x \\ z \end{bmatrix} = \begin{bmatrix} \cos(\theta) & \sin(\theta) \\ -\sin(\theta) & \cos(\theta) \end{bmatrix} \cdot \begin{bmatrix} \bar{x} \\ \bar{z} \end{bmatrix} \qquad (1)$$

leading to permeability at arbitrary angle θ [29]:

$$k(\theta) = k_z \sin^2(\theta) + k_x \cos^2(\theta). \qquad (2)$$

Because the range of possible measurement angles is symmetric, Eq. 2 describes an ellipse.

Despite the well-established theoretical basis and observations of anisotropy across scales in volcanic settings, the consequences of considering nonisotropic permeability in volcanic contexts are poorly constrained. Key questions include the extent to and direction in which fluid flow is deflected in such systems, and how this affects processes like outgassing and pressurisation. Here, the directional dependence of permeability is quantified through systematically varied angular sampling of

EarthArXiv preprint

transversely isotropic volcanic tuff. The results are used to derive an analytical framework then applied to four case study settings where flow deflection has direct implications for eruption dynamics, volcanic hazards, regional-scale fluid movement, and physical magmatic processes.

2 Materials and Methods

Samples were prepared from a block of Fukumitsu-ishi volcanic tuff, quarried in Shimane Prefecture (Japan),deposited as part of the volcanic succession of the Miocene-age Kuri Formation [33]. Fukumitsu-ishi is a fine-textured rhyolitic lapilli tuff composed of plagioclase, quartz, and biotite (altered to chlorite) forming a glass-shard and crystal matrix [33,34]. In hand sample it appears eutaxitic, with flattened pumice, fiamme, strongly oblate vesicles, and igneous and mudstone lithic fragments (Figure 1c). Visual inspection reveals transverse isotropy, such that $x = y \neq z$.

Cylinders of 25 mm diameter were cored with respect to visible fabric (Figure 1c). Samples were obtained at angles of 0, 18, 36, 54, 72, and 90° ($\theta \in [0, \ldots, 0.5]\pi$ rad), then ground flat and parallel to ~50 mm and dried under vacuum for 48+ hours. Permeability was measured using a custom-built gas permeameter (Figure 1a, b). A full description of the apparatus, its operation, and the data collection and analysis are given in Supporting Information Text S1.

EarthArXiv preprint

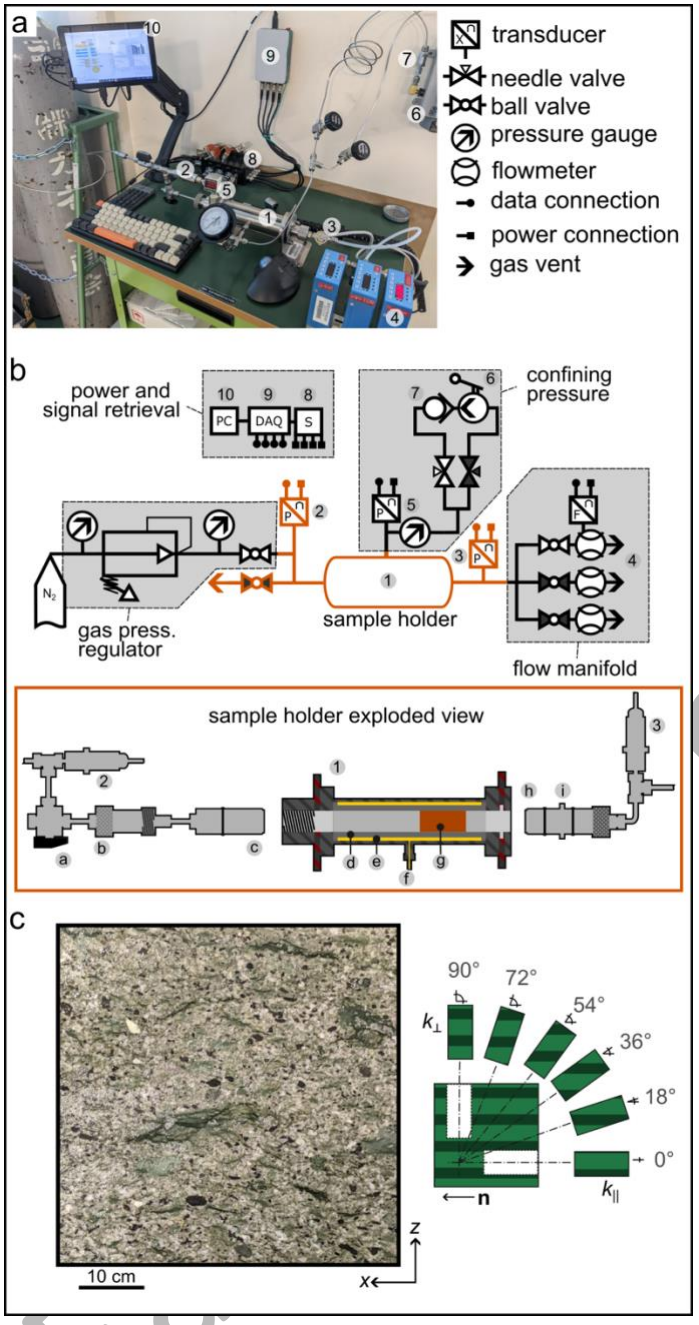


Figure 1. a) Gas permeameter: 1, sample core holder; 2, upstream pressure transducer; 3, downstream pressure transducer; 4, flow meter manifold; 5, confining pressure gauge; 6, confining pressure pump; 7, check valve; 8, switch box; 9, data acquisition module; 10, LabVIEW program. b) Schematic of (a) with exploded sample holder view: a, upstream vent; b, knurled screw; c, upstream platen; d, Viton sleeve; e, confining fluid; f, confining fluid inlet/outlet; g, sample; h, downstream platen; i, bayonet connector. c) Sawcut of Fukumitsu-ishi tuff showing defined x and z planes and sample retrieval strategy.

Preprint

3 Results

Figure 2a shows permeability of Fukumitsu-ishi tuff samples as a function of coring angle. Extrema are 2.845 $\times 10^{-17}$ and 1.149 $\times 10^{-17}$ m^2 respectively at $\theta = 0$ and 0.5π rad. Full data are given in Table 1. In Figure 2b, these data are plotted in radial coordinates ($1/\sqrt{k}$ vs. θ). Two ellipse-fitting approaches are considered. The first is a principal-axis model (dashed line, Figure 2a, 2b): $k(\theta) = \langle k_z \rangle \sin^2\theta + \langle k_x \rangle \cos^2\theta$, derived from rotation of the permeability tensor as described above, where $\langle k_x \rangle$ and $\langle k_z \rangle$ denote equivalent permeability values calculated as the average of $n = 2$ samples obtained at 0 and 0.5π rad respectively: $\langle k_x \rangle = \frac{1}{n}\sum_{i=1}^{n} k_i$ and $\langle k_z \rangle = \left(\frac{1}{n}\sum_{i=1}^{n} k_i^{-1}\right)^{-1}$. The second approach is a full tensor regression (solid ellipse), in which the tensor components are estimated by linear least-squares regression using directional permeability measurements at all orientations, without prescribing the orientation of the principal axes. The anisotropy ratio $A_k = \langle k_x \rangle / \langle k_z \rangle$ is 2.25 for the sample suite. The principal-axis model sufficiently describes the data: the full tensor regression model returns principal axes within 1° of the prescribe coring direction (Figure 2 inset), confirming the assumed fabric orientation. Where the principal axes are not known a priori, a full regression approach should prove more appropriate.

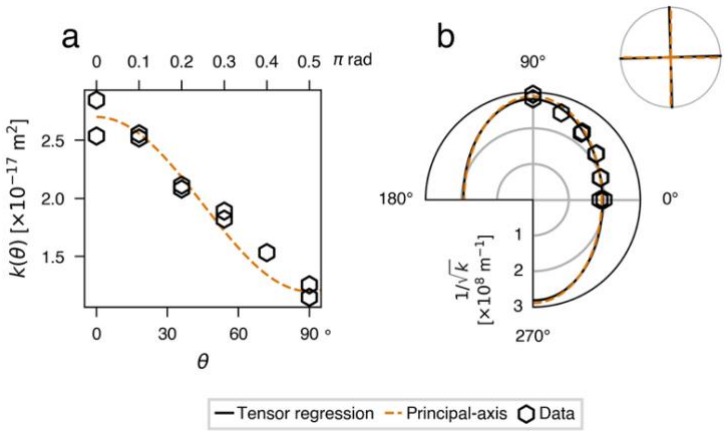


Figure 2. a) Fukumitsu tuff permeability k vs. core angle θ; dashed line, principal-axis model. b) Permeability in radial coördinates ($1/\sqrt{k}$ vs. θ). Dashed ellipse, principal-axis model; solid ellipse, full tensor regression model. Inset: principal axes orientation for each model.

Table 1: Uncorrected and correct permeability measurements for Fukumitsi-ishi tuff samples cored at various angles with respect to fabric.

Sample	Permeability (m^2)		Angle (°)
	Darcian k_D	Klinkenberg-corrected k_K	
Fuku-00-A	4.83E-17	2.845E-17	0
Fuku-00-B	4.62E-17	2.536E-17	0
Fuku-18-A	4.29E-17	2.555E-17	18
Fuku-18-B	4.40E-17	2.519E-17	18

Earth and Space Science Open Archive preprint

Fuku-36-A	3.92E-17	2.080E-17	36
Fuku-36-B	3.79E-17	2.113E-17	36
Fuku-54-A	3.11E-17	1.890E-17	54
Fuku-54-B	2.73E-17	1.821E-17	54
Fuku-72	2.70E-17	1.533E-17	72
Fuku-90-A	2.20E-17	1.149E-17	90
Fuku-90-B	2.33E-17	1.256E-17	90
$\langle k_x \rangle$	-	2.700E-17	0
$\langle k_z \rangle$	-	1.200E-17	90

4 Discussion

4.1 Flow deflection

The departure of the pore network from the isotropic identity $\mathbf{K} = k\mathbf{I}$ is encapsulated by the anisotropy ratio A_k; once a dominant structural axis $\mathbf{n}$ exists, that departure can be derived in closed form. For any anisotropy $A_k \neq 1$, flow is deflected from the imposed hydraulic gradient: flow direction through a transversely isotropic medium can only coincide with the hydraulic gradient orientation along the principal axes of the tensor ellipse [35], as shown in Figure 3a for A_k = 2.25 (as in 1b). Let β denote the angle $0 < \beta < \pi/2$ between the pressure-gradient vector and the principal axis of maximum permeability (k_x), and α denote the angle between the Darcy flux vector and the same axis. The deflection $\delta = \beta - \alpha$ is then the angular deviation between the imposed gradient and the resulting flow direction. Flow deflection is governed by the expression $\alpha = \arctan(\tan\beta / A_k)$ [36]; so:

$$\delta = \beta - \arctan(\tan\beta / A_k) \quad (3)$$

Eq. 3 describes the surface shown in Figure 3b. Differentiating with respect to β yields

$$\frac{d(\delta)}{d\beta} = 1 - \frac{A_k \sec^2\beta}{A_k^2 + \tan^2\beta} \quad (4)$$

Setting Eq. 4 equal to zero gives $A_k^2 + \tan^2\beta = A_k(1 + \tan^2\beta)$, which simplifies to $\tan^2\beta = A_k$ while $A_k \neq 1$. So,

$$\beta^* \stackrel{\text{def}}{=} \underset{\beta}{\operatorname{argmax}}(\delta) = \arctan\left(\sqrt{A_k}\right) \quad (5)$$

which substitutes into (3), using the identity $\arctan(x) + \arctan(1/x) = (\pi/2)$, to yield:

EarthArXiv preprint

$$\delta^* \stackrel{\text{def}}{=} \max_{\beta}(\delta) = 2\arctan(\sqrt{A_k}) - (\pi/2) \quad (6).$$

β^* is the critical gradient angle: the orientation of the hydraulic gradient relative to $\mathbf{n}$ at which flow deflection reaches its maximum value δ^*. The closed-form expression (5) shows that the pressure-gradient orientation producing the maximum flow deflection depends only on A_k; further, Eq. 6 demonstrates that the maximum deflection is a monotonic function of A_k which approaches $\pi/2$ rad (90°) asymptotically as anisotropy increases (shown graphically in Figure 3c). From the analytical solutions derived here it becomes straightforward to define the angle of maximum deflection given the magnitude of anisotropy, or vice versa.

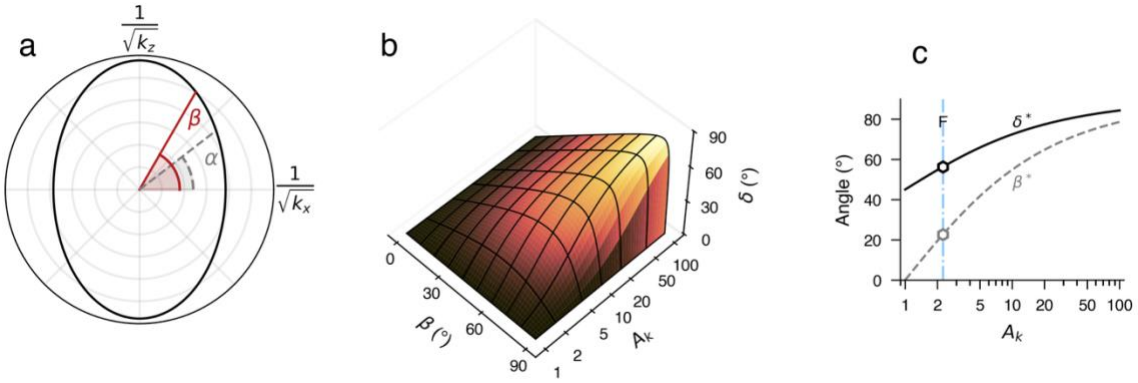


Figure 3. a) Permeability ellipse for A = 2.25, showing pressure-gradient vector β (solid line) and the angle of maximum flow velocity α (dashed line). b) 3-dimensional surface described by angles β and δ, and anisotropy A_k. c) Equations 5 (solid) and 6 (dashed); hexagons show calculated values for Fukumitsu-ishi (F).

4.2 Applications and implications

4.2.1 Volcanic conduit margin anisotropy

In the case of conduit margin shear, $\mathbf{n}$ is parallel to the conduit wall. Gaunt et al. [37] report permeability anisotropy in Mount St. Helens (USA) spine samples: at the margin, $A_k \sim 10^3$, dominated by vertical, shear-parallel permeability, yielding $\beta^* \sim 88°$ and $\delta^* \sim 86°$. Even a driving gradient oriented near-orthogonal to $\mathbf{n}$ would yield a flux vector only $\alpha^* = \beta^* - \delta^* = 2°$ from $\mathbf{n}$ (vertical): strong anisotropy renders flow essentially insensitive to the gradient orientation. In the massive core $A_k < 1$ (i.e. k_x and k_z switch sense relative to the margin), deflecting fluid laterally instead—consistent with strong marginal anisotropy channelling fluids out and to the surface [37]. By contrast, in the high-shear marginal zone of Unzen volcano (Japan), Lavallée et al. [38] measure $A_k \sim 2–3$, giving values of $\beta^* \sim 55–60°$ and $\delta^* \sim 19–30°$: flow remains vertically biased but far less tightly channeled. This sensitivity to the hydraulic gradient orientation is particularly important given the oblique inclination of the Unzen conduit [39].

EarthArXiv preprint

4.2.2 Fumarole field offsets

Equations 5 and 6 imply that oblique fluid flow architecture in the volcanic subsurface will deflect outgassing/upwelling fluids, creating a lateral offset Ω between the fluid source and its surface expression (e.g. fumaroles). With a uniform gradient and ideal transverse isotropy, this offset equals $\Omega = \mathcal{d}\tan(\delta)$, where $\mathcal{d}$ is the distance along the imposed hydraulic gradient. Pearson et al. model fluid flow at Masaya volcano through a permeable (10^{-12} m^2) host rock overprinted by a relatively less permeable (10^{-16} m^2) fault system dipping 60° from horizontal: geometrically equivalent to a transversely isotropic medium with $A_k = 10^4$ and β = 30°. Eq. 3 yields $\alpha \sim 0.003°$; as with the Mount St. Helens case, high anisotropy means flow is strongly coupled to the fault-parallel axis, governed by the fault dip. From $\mathcal{d}$ = 125 m (the depth at which the modeled faults intersect with the permeable domain), the predicted horizontal fluid flux offset would be $\Omega \sim 72$ m. The full numerical solution [40] predicts enhanced fluid flux ~30–70 m towards the fault footwall from the source at that depth. This agreement indicates that the fluid deflection, captured by the simple analytical form, exerts a first-order control on the surface expression of subsurface fluid movement in the system.

4.2.3 Flow deflection at the regional scale

At the regional scale, the migration of fluid through volcanic and geothermal systems—governed by regional fault systems [11,12]—controls the location and nature of hydrothermal alteration [41]; the spatial distribution of economic resources [42]; and the surface expression of magmatic activity [43]. Tracer tests in the Awibengkok geothermal field (Indonesia) by Gunderson et al. [44] reveal flow deflection up to 75° from the prevailing pressure gradient. The corollary of Eq. 6 is that $\sqrt{A_k} = \tan([\delta^*/2] + [\pi/4])$. Through tangent addition this simplifies to the closed form:

$$A_k = \left(\frac{1+\tan(\delta^*/2)}{1-\tan(\delta^*/2)}\right)^2 \quad (7).$$

The reported deflection at Awibengkok thus reflects an anisotropy ratio for the geothermal field of $A_k \sim 58$. Equation 7 therefore offers a route for retrieving equivalent bulk anisotropy as a function of the observed deflection angle δ^*: translating observable quantities into a constitutive parameter to constrain subsurface fluid flow modelling.

4.2.4 Flow deflection in compacting magma

A final example considers dynamic anisotropy. Ashwell et al. [14] experimentally deform Ngongotaha Pumiceous (NP) and Tarawera Dense (TD) magmas, measuring axial k_{ax} and radial k_{rad} permeability after varying amounts of compaction. Taking A_k as k_{ax}/k_{rad} reveals differing patterns of anisotropy evolution (Figure 4a): crystal-poor NP magma shows a reversal in the sense of anisotropy as compaction proceeds. Equation 6 yields the corresponding evolution of δ^* with porosity ϕ (Figure 4b). The crystalline TD samples exhibit $A_k \gg 1$ throughout the porosity range; δ^* remains high and relatively stable (~87–89º). In contrast, for NP magma, δ^* decreases from 89.7º at $\phi = 0.58$ to −89.9º at $\phi = 0.28$, passing through the isotropic limit $A_k = 1, \delta^* = 0$ at $0.39 > \phi > 0.30$. Thus, the direction of preferential flow rotates by 90º during

EarthArXiv preprint

compaction: fluids are deflected towards the compaction axis at high ϕ but deflected perpendicular to compaction as ϕ decreases. Reorganisation of preferential pathways has implications for gas escape during compaction and welding, which are pervasive in volcanic deposits and conduits [45]. More broadly, the permeability tensor can evolve dramatically even as porosity changes monotonically, meaning a scalar model calibrated at a single porosity incompletely samples the complex evolution of permeability anisotropy. Capturing this evolution is crucial for developing accurate models of fluid escape during magma compaction and welding.

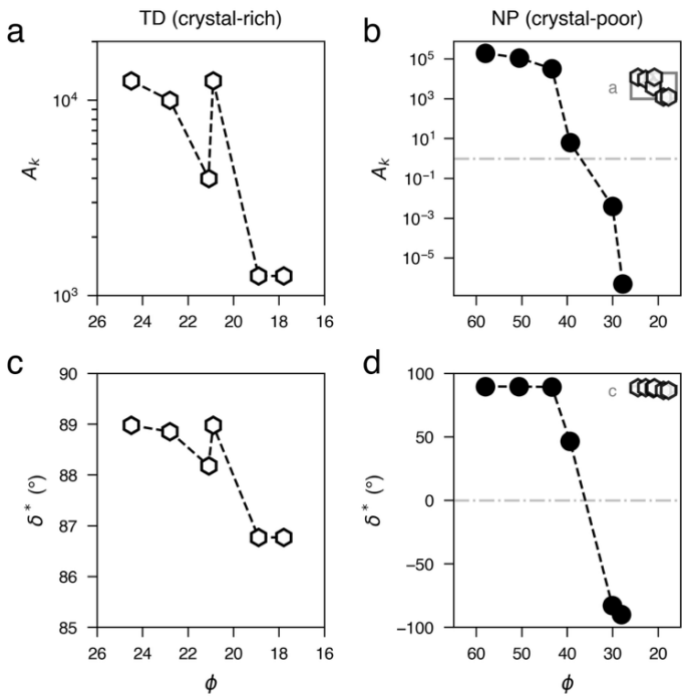


Figure 4. a–b) Anisotropy k_{ax}/k_{rad} of Tarawera Dense (TD) and Ngongotaha Pumiceous (NP) samples (Ashwell et al., 2015) vs. decreasing porosity ϕ; inset in a: axis range of TD samples in a. Dot-dash line in B shows $A_k = 1$, the isotropic limit. c–d) Maximum fluid flow deflection angle δ^* from a–b. Dot-dash line in D: $\delta^* = 0$, zero deflection.

5 Conclusions

Permeability anisotropy exerts a first-order control on the direction of fluid transport in volcanic systems. This contribution derives closed-form analytical relations that directly link permeability anisotropy to the magnitude and angle of flow deflection from the hydraulic gradient, providing an analytical framework for determining fluid migration in transversely isotropic media. These solutions are applied to cases studies demonstrating that anisotropy can significantly redirect fluid transport, enhancing conduit outgassing and creating lateral offsets in the surface expression of ascending magmatic fluids. Using this framework, observed flow deflections at the field-scale can be used to determine effective bulk anisotropy. Further, evolving anisotropy is shown to fundamentally redirect preferential flow routes in compacting magma. These results

Earth... Preprint

emphasise that accounting for directional dependence is crucial for understanding fluid flow through volcanic and hydrothermal systems across all scales.

Acknowledgments

Sample materials were obtained from Nichika Co. Ltd. (Japan). Alex Kushnir is thanked for early development of the pulse-decay code; Kaja Fenn for proofreading. JIF was funded by Niigata University (project 543142: Promotion of advanced research by the Institute for Research Administration) with additional support from JSPS Grant-in-Aid for Scientific Research(B) 24K00730.

Data accessibility statement

Data are provided in Table 1, and all Python code necessary to repeat the analyses and plotting are provided at the following archived repository: DOI: 10.5281/zenodo.22821868.

Conflict of Interest Disclosure

The author declares there are no conflicts of interest for this manuscript.

Author contributions

JIF conducted all aspects of this study, including conceptualisation, data collection, analysis, and manuscript preparation.

References

1. Ingebritsen SE, Gleeson T. 2015 Crustal permeability: Introduction to the special issue. *Geofluids* **15**, 1–10. (doi:10.1111/gfl.12118)

2. Manga M, Beresnev I, Brodsky EE, Elkhoury JE, Elsworth D, Ingebritsen SE, Mays DC, Wang C. 2012 Changes in permeability caused by transient stresses: Field observations, experiments, and mechanisms. *Reviews of Geophysics* **50**, 2011RG000382. (doi:10.1029/2011RG000382)

3. Ingebritsen SE, Manning CE. 2010 Permeability of the continental crust: dynamic variations inferred from seismicity and metamorphism. *Geofluids* **10**, 193–205. (doi:10.1111/j.1468-8123.2010.00278.x)

EarthArXiv preprint

4. Heap MJ, Farquharson JI, Wadsworth FB, Kolzenburg S, Russell JK. 2015 Timescales for permeability reduction and strength recovery in densifying magma. *Earth and Planetary Science Letters* **429**, 223–233. (doi:10.1016/j.epsl.2015.07.053)

5. Farquharson JI, Wadsworth FB, Heap MJ, Baud P. 2017 Time-dependent permeability evolution in compacting volcanic fracture systems and implications for gas overpressure. *Journal of Volcanology and Geothermal Research* **339**, 81–97. (doi:10.1016/j.jvolgeores.2017.04.025)

6. Cassidy M, Manga M, Cashman K, Bachmann O. 2018 Controls on explosive-effusive volcanic eruption styles. *Nat Commun* **9**, 2839. (doi:10.1038/s41467-018-05293-3)

7. Collinson ASD, Neuberg JW. 2012 Gas storage, transport and pressure changes in an evolving permeable volcanic edifice. *Journal of Volcanology and Geothermal Research* **243–244**, 1–13. (doi:10.1016/j.jvolgeores.2012.06.027)

8. Diller K, Clarke AB, Voight B, Neri A. 2006 Mechanisms of conduit plug formation: Implications for vulcanian explosions. *Geophysical Research Letters* **33**, 2006GL027391. (doi:10.1029/2006GL027391)

9. Farquharson JI, Heap MJ, Lavallée Y, Varley NR, Baud P. 2016 Evidence for the development of permeability anisotropy in lava domes and volcanic conduits. *Journal of Volcanology and Geothermal Research* **323**, 163–185. (doi:10.1016/j.jvolgeores.2016.05.007)

10. Clavaud J-B, Maineult A, Zamora M, Rasolofosaon P, Schlitter C. 2008 Permeability anisotropy and its relations with porous medium structure. *Journal of Geophysical Research: Solid Earth* **113**. (doi:10.1029/2007JB005004)

11. Hutchison W, Mather TA, Pyle DM, Biggs J, Yirgu G. 2015 Structural controls on fluid pathways in an active rift system: A case study of the Aluto volcanic complex. *Geosphere* **11**, 542–562. (doi:10.1130/GES01119.1)

12. Hughes EC, Mazot A, Kilgour G, Asher C, Michelini M, Britten K, Chardot L, Feisel Y, Werner C. 2019 Understanding Degassing Pathways Along the 1886 Tarawera (New Zealand) Volcanic Fissure by Combining Soil and Lake CO2 Fluxes. *Front. Earth Sci.* **7**. (doi:10.3389/feart.2019.00264)

13. Wright HMN, Roberts JJ, Cashman KV. 2006 Permeability of anisotropic tube pumice: Model calculations and measurements. *Geophysical Research Letters* **33**. (doi:10.1029/2006GL027224)

14. Ashwell PA, Kendrick JE, Lavallée Y, Kennedy BM, Hess K-U, von Aulock FW, Wadsworth FB, Vasseur J, Dingwell DB. 2015 Permeability of compacting porous lavas. *Journal of Geophysical Research: Solid Earth* **120**, 1605–1622. (doi:10.1002/2014JB011519)

EarthArXiv preprint

15. Wright HMN, Cashman KV, Gottesfeld EH, Roberts JJ. 2009 Pore structure of volcanic clasts: Measurements of permeability and electrical conductivity. *Earth and Planetary Science Letters* **280**, 93–104. (doi:10.1016/j.epsl.2009.01.023)

16. Bayramov K, Heap MJ, Baud P, Hasanov AB. 2026 The control of pore geometry and orientation on compaction localization in triaxially deformed porous lava. *Journal of Structural Geology* **211**, 105777. (doi:10.1016/j.jsg.2026.105777)

17. Bear J. 1972 *Dynamics of Fluids in Porous Media*.

18. Whitaker S. 1986 Flow in porous media I: A theoretical derivation of Darcy's law. *Transp Porous Med* **1**, 3–25. (doi:10.1007/BF01036523)

19. Whitaker S. 2013 *The Method of Volume Averaging*. Springer Science & Business Media.

20. Okumura S, Nakamura M, Tsuchiyama A, Nakano T, Uesugi K. 2008 Evolution of bubble microstructure in sheared rhyolite: Formation of a channel-like bubble network. *J. Geophys. Res.* **113**, 2007JB005362. (doi:10.1029/2007JB005362)

21. Birnbaum J, Schauroth J, Weaver J, Kendrick JE, Lamur A, Lavallée Y. 2026 Shear-enhanced dynamic permeability development of magma vesiculating in cylindrical conduits. *Sci Rep* **16**, 9838. (doi:10.1038/s41598-026-43344-8)

22. Taylor-West J, Katz RF. 2015 Melt-preferred orientation, anisotropic permeability and melt-band formation in a deforming, partially molten aggregate. *Geophys J Int* **203**, 1253–1262. (doi:10.1093/gji/ggv372)

23. Okumura S, Nakamura M, Nakano T, Uesugi K, Tsuchiyama A. 2010 Shear deformation experiments on vesicular rhyolite: Implications for brittle fracturing, degassing, and compaction of magmas in volcanic conduits. *Journal of Geophysical Research: Solid Earth* **115**. (doi:10.1029/2009JB006904)

24. Wright HM, Cashman KV. 2014 Compaction and gas loss in welded pyroclastic deposits as revealed by porosity, permeability, and electrical conductivity measurements of the Shevlin Park Tuff. *Geological Society of America Bulletin* **126**, 234–247. (doi:10.1130/B30668.1)

25. Závada P, Schulmann K, Lexa O, Hrouda F, Haloda J, Týcová P. 2009 The mechanism of flow and fabric development in mechanically anisotropic trachyte lava. *Journal of Structural Geology* **31**, 1295–1307. (doi:10.1016/j.jsg.2009.04.002)

26. Colombier M, Wadsworth FB, Gurioli L, Scheu B, Kueppers U, Di Muro A, Dingwell DB. 2017 The evolution of pore connectivity in volcanic rocks. *Earth and Planetary Science Letters* **462**, 99–109. (doi:10.1016/j.epsl.2017.01.011)

EarthArXiv preprint

27. Stanton-Yonge A, Mitchell TM, Healy D, Meredith PG, Browning J, Adamus F. 2026 The anisotropy of permeability under simulated crustal stress conditions: Experimental evidence of flow enhancement parallel to the intermediate principal stress. *Geology* (doi:10.1130/G54686.1)

28. Manga M, Stone HA. 1994 Interactions between bubbles in magmas and lavas: effects of bubble deformation. *Journal of Volcanology and Geothermal Research* **63**, 267–279. (doi:10.1016/0377-0273(94)90079-5)

29. Farquharson JI, Wadsworth FB. 2018 Upscaling permeability in anisotropic volcanic systems. *Journal of Volcanology and Geothermal Research* **364**, 35–47. (doi:10.1016/j.jvolgeores.2018.09.002)

30. Kendrick JE *et al.* 2021 Physical and mechanical rock properties of a heterogeneous volcano: the case of Mount Unzen, Japan. *Solid Earth* **12**, 633–664. (doi:10.5194/se-12-633-2021)

31. Vairé E, Heap MJ, Baud P, van Wyk de Vries B. 2024 Quantifying the physical and mechanical heterogeneity of porous volcanic rocks from the Chaîne des Puys (Massif Central, France). *Bull Volcanol* **86**, 49. (doi:10.1007/s00445-024-01742-8)

32. Bernard M-L, Zamora M, Géraud Y, Boudon G. 2007 Transport properties of pyroclastic rocks from Montagne Pelée volcano (Martinique, Lesser Antilles). *Journal of Geophysical Research: Solid Earth* **112**. (doi:10.1029/2006JB004385)

33. Takasu A. 2009 Fukumitsu Stone in Onsen-tsu. *100 Selected Shimane Geosites (Iwami Region)*. See https://www.geo.shimane-u.ac.jp/geopark/fukumitsuishi.html? (accessed on 23 August 2026).

34. Kano K, Takarada S, Makimoto H, Tsuchiya N, Yutaka H. 2001 Geology of the Onsenzu and Gotsu Regions. *Regional Geological Research Reports; 1:50,000 Geological Map Sheets [Okayama]* **12**.

35. Liakopoulos AC. 1965 Darcy's Coefficient of Permeability as Symmetric Tensor of Second Rank. *International Association of Scientific Hydrology. Bulletin* **10**, 41–48. (doi:10.1080/02626666509493405)

36. Krizek RJ. 1968 PERMEABILITY OF ANISOTROPIC POROUS MEDIA. *Highway Research Record*

37. Gaunt HE, Sammonds PR, Meredith PG, Smith R, Pallister JS. 2014 Pathways for degassing during the lava dome eruption of Mount St. Helens 2004–2008. *Geology* **42**, 947–950. (doi:10.1130/G35940.1)

38. Lavallée Y *et al.* 2022 Transient conduit permeability controlled by a shift between compactant shear and dilatant rupture at Unzen volcano (Japan). *Solid Earth* **13**, 875–900. (doi:10.5194/se-13-875-2022)

Earth ArXiv preprint

39. Umakoshi K, Takamura N, Shinzato N, Uchida K, Matsuwo N, Shimizu H. 2008 Seismicity associated with the 1991–1995 dome growth at Unzen Volcano, Japan. *Journal of Volcanology and Geothermal Research* **175**, 91–99. (doi:10.1016/j.jvolgeores.2008.03.030)

40. Pearson SCP, Kiyosugi K, Lehto HL, Saballos JA, Connor CB, Sanford WE. 2012 Integrated geophysical and hydrothermal models of flank degassing and fluid flow at Masaya volcano, Nicaragua. *Geochemistry, Geophysics, Geosystems* **13**. (doi:10.1029/2012GC004117)

41. Rossetti F, Aldega L, Tecce F, Balsamo F, Billi A, Brilli M. 2011 Fluid flow within the damage zone of the Boccheggiano extensional fault (Larderello–Travale geothermal field, central Italy): structures, alteration and implications for hydrothermal mineralization in extensional settings. *Geological Magazine* **148**, 558–579. (doi:10.1017/S001675681000097X)

42. Wilkinson JJ. 2013 Triggers for the formation of porphyry ore deposits in magmatic arcs. *Nature Geosci* **6**, 917–925. (doi:10.1038/ngeo1940)

43. Edmonds M, Oppenheimer C, Pyle DM, Herd RA, Thompson G. 2003 SO2 emissions from Soufrière Hills Volcano and their relationship to conduit permeability, hydrothermal interaction and degassing regime. *Journal of Volcanology and Geothermal Research* **124**, 23–43. (doi:10.1016/S0377-0273(03)00041-6)

44. Gunderson R, Rosa S, Sirad-Azwar L. 2002 Fluorescein and naphthalene sulfonate liquid tracer results at the Awibengkok geothermal field, West Java, Indonesia. *Proceedings, 27th Workshop on Geothermal Reservoir Engineering* **28**.

45. Quane SL, Russell JK, Friedlander EA. 2009 Time scales of compaction in volcanic systems. *Geology* **37**, 471–474. (doi:10.1130/G25625A.1)

EarthArXiv preprint

420

EarthArXiv preprint